communications materials

A Nature Portfolio journal

Article

https://doi.org/10.1038/s43246-025-00995-w

Overcoming drug resistance microspheres combined with photothermal ablation reinforce transcatheter arterial chemoembolization of hepatocellular carcinoma

Jiheng Shan[1,2,7], Chengzhi Zhang[1,2,7], Yiming Liu[1,2], Bingtong Yue[1,2], Bin Han[1,3], Jing Li[1,2], Guodun Zheng[1,2], Kunpeng Wu[1,2], Huijuan Wu[1,3], Yiran Wang[1,2], Qingqing He[1,2], Xiaonan Shan[4], Zongming Li[1,2], Ping Wu[5], Kewei Ren[1,2], Zhen Li[1,2], Jianzhuang Ren[1,2,8] ✉, Linyong Du[6] ✉, Yanan Zhao[1,2] ✉ & Xinwei Han[1,2,8] ✉

Drug-eluting microspheres (DEMs) are key for transcatheter arterial chemoembolization (TACE) in advanced hepatocellular carcinoma (HCC), but face challenges like tumor multidrug resistance (MDR) and poor post-TACE outcomes. Here we show a dual-effect microsphere (PTIMS) co-encapsulating idarubicin (IDA) and tariquidar (TQR) for simultaneous chemotherapy and MDR reversal, plus minimally invasive photothermal therapy (PTT) to boost antitumor efficacy. Physicochemical tests confirm IDA/TQR loading in PTIMS, with PTT accelerating drug release. In vitro, PTIMS-PTT strongly inhibits H22 cell proliferation, migration and invasion by downregulating membrane P-glycoprotein (P-gp), promoting apoptosis and reducing IDA efflux. In vivo, it suppresses tumor growth in murine H22 models (upregulating TNF-α, downregulating Ki67/P-gp) and inhibits progression in rabbit VX2 liver tumors via robust embolization. PTIMS offers a promising strategy to enhance TACE efficacy, with high clinical translation potential.

Liver cancer ranks as the sixth most prevalent cancer globally, with hepatocellular carcinoma (HCC) comprising ~90% of cases[1,2]. Current therapeutic strategies for HCC include liver transplantation, local ablation therapy, systemic treatment and transcatheter arterial chemoembolization (TACE)[3], with TACE widely recognized as an effective approach for advanced HCC[4]. The efficacy of drug-eluting microspheres (DEMs) is pivotal in determining patient outcomes following TACE, serving as a cornerstone of the procedure[5].

DEMs should possess three key characteristics: efficient targeted drug delivery to tumor tissues, uniform particle sizes compatible with target vascular diameters, and effective imaging capabilities for postoperative efficacy monitoring[6]. In recent decades, commercial DEM such as DC Beads®, HepaSpheres® and CalliSpheres® have been successively introduced[7]. Owing to their capacity to achieve local high drug concentrations, ensure complete vascular embolization and facilitate stable, sustained drug release, these microspheres have progressively replaced conventional iodized oil embolic agents[8] as the preferred choice for TACE. Most currently used DEMs rely on cation-anion exchange mechanisms for drug loading[9,10]. However, the drug loading efficiency is compromised owing to the limited drug-loading capacity and the potential for interactions among multiple drugs during the

[1]Department of Interventional Radiology, Key Laboratory of Interventional Radiology of Henan Province, The First Affiliated Hospital of Zhengzhou University, Zhengzhou, China. [2]Interventional Institute of Zhengzhou University, Zhengzhou, China. [3]Department of Radiation Oncology, The First Affiliated Hospital of Zhengzhou University, Zhengzhou, China. [4]Institute of Laser Manufacturing, Henan Academy of Sciences, Zhengzhou, China. [5]Oujiang Laboratory (Zhejiang Lab for Regenerative Medicine, Vision and Brain Health), School of Pharmaceutical Science, Wenzhou Medical University, Wenzhou, China. [6]Key Laboratory of Medicine, Ministry of Education of China, School of Laboratory Medicine and Life Science, Wenzhou Medical University, Wenzhou, Zhejiang, China. [7]These authors contributed equally: Jiheng Shan, Chengzhi Zhang. [8]These authors jointly supervised this work: Jianzhuang Ren, Xinwei Han. ✉e-mail: rjzjrk@126.com; dulinyong@msn.com; yananzhao996@163.com; fcchanxw@zzu.edu.cn

loading process. To address these challenges, our previous research has successfully developed polydopamine (PDA)-coated microspheres with high drug-loading efficiency for multiple drugs[11].

Photothermal therapy (PTT) represents an innovative and minimally invasive modality for tumor thermal ablation[12]. This approach uses photothermal conversion agents (PTAs) to convert near-infrared (NIR) light energy into heat, elevating tissue temperature to induce tumor cell apoptosis[13]. Presently, PTAs, such as noble metal materials, carbon-based nanomaterials and other two-dimensional materials (e.g., black phosphorus nanosheets, boron nitride and MXenes) have demonstrated exceptional efficacy in PTT for tumors[14,15]. Yet PTT advancement is hindered by high production costs, complex manufacturing, and potential biotoxicity[16]. PDA, synthesized via dopamine oxidation and self-polymerization, exhibits superior photothermal conversion efficiency. Additionally, its notable adhesive properties, excellent biocompatibility, and photothermally responsive drug release characteristics have attracted significant scientific attention[17,18]. Contemporary PTT offers the advantages of minimal invasiveness, precision, low adverse reaction rates and high specificity[19], making it suitable for minimally invasive post-TACE photothermal treatment. This efficacy stems from PTT's ability to induce cancer cell apoptosis, locally release tumor-specific antigens, initiate specific anti-tumor immune responses and enhance the tumor immune microenvironment[20]. Moreover, PTT augments chemotherapy sensitivity by inhibiting the function of drug efflux pumps on the tumor cell membrane through temperature elevation[21,22].

Anthracyclines such as doxorubicin, pirarubicin and idarubicin (IDA)[23,24], have become widely adopted in TACE as effective chemotherapeutic agents with promising application prospects[25]. As cell cycle-specific chemotherapy drugs, anthracyclines exhibit potent anti-proliferative effects against various tumor types[26] and can enhance the tumor immune microenvironment, recruiting activated cytotoxic T lymphocytes to the tumor site[27]. Among them, IDA has garnered attention for its advantageous lipophilicity, prolonged biological half-life and reduced cardiotoxicity. However, multidrug resistance (MDR) frequently challenges monotherapy outcomes[28]. The primary mechanism of drug resistance involves P-glycoprotein (P-gp)-mediated active efflux of chemotherapeutics (e.g., paclitaxel, doxorubicin, idarubicin) from tumor cells[29,30], reducing intracellular drug concentrations and limiting IDA efficacy[31]. Tariquidar (TQR), a chemosensitizer and specific P-gp inhibitor, shows high affinity towards P-gp[32–34]. By inducing the transition of P-gp from its closed conformation to an open conformation, it impedes the binding of P-gp to substrates and diminishes its efflux effect on anticancer drugs, consequently restoring the chemosensitivity of tumor cells[35]. Therefore, the integration of IDA and TQR holds promise to enhance the efficacy of tumor treatment.

Herein, the aim of this study was to develop dual-effect embolized microspheres integrated with photothermal ablation for the treatment of HCC via TACE. As illustrated in Fig. 1a, IDA and TQR were simultaneously loaded onto PDA-coated polycinyl alcohol (PVA) microspheres to develop PTIMS. These microspheres were subsequently applied to both the Balb/c mouse subcutaneous H22 transplanted tumor model and the New Zealand rabbit VX2 liver tumor model. Specifically, the subcutaneous mouse model serves as a proof-of-concept system to isolate the effects of PTIMS from the complexities of tumor vasculature, providing mechanistic insights into drug release, photothermal ablation, and MDR reversal. These findings lay the foundation for translating PTIMS into TACE applications in orthotopic liver tumor models. As depicted in Fig. 1b, PTIMS function as embolic agents in TACE procedures. They not only obstruct the blood supply to the tumor and facilitate localized drug release within the tumor, but also function as a heat source for minimally invasive photothermal ablation following TACE, thereby further enhancing drug release and improving bioavailability. This PTIMS-PTT combined modality promotes apoptosis of tumor cells, inhibits their migration and invasion, and enhances the immune microenvironment. Importantly, this combination therapy exhibits a cascade amplification effect, characterized by reduced P-gp expression and increased IDA uptake in tumor cells, significantly improving the therapeutic efficacy of HCC.

Results

Physicochemical properties

The double-effect PVA microspheres coated with PDA were successfully prepared, as confirmed by Raman spectroscopy analysis (Fig. 2a, b and Supplementary Fig. 1). The results indicate that the characteristic peaks of PDA appear at 1369 and 1568 cm^{-1}, which correspond to the deformation and stretching vibrations of catechol groups within PDA[36,37]. Additionally, the characteristic peaks of TQR and IDA were observed at 1302 and 1599 cm^{-1}, and at 2675 and 3708 cm^{-1}, respectively. These PDA-specific peaks were detected in PMS, PTMS, PIMS, and PTIMS, confirming the successful coating of PDA on the surface of PVA microspheres. However, the characteristic peaks of TQR and IDA were not detected in PTMS, PIMS, and PTMR. This phenomenon may be attributed to the formation of hydrogen bonds or π–π stacking interactions between PDA molecules, which contain multiple phenolic hydroxyl groups, and IDA or TQR molecules, leading to changes in their vibrational modes. Therefore, the Zeta potential test was implemented further. It can be seen from Fig. 2c that the Zeta potential of PVA, PDA and TQR is negative, while that of IDA is positive. The Zeta potential of PMS (-22.73 ± 0.48 mV) tends to be negative compared with that of PVA (-5.10 ± 0.32 mV), indicating that the PMS surface is successfully coated with PDA. Analogously, the Zeta potential of PIMS (-9.92 ± 0.36 mV) and PTIMS (-10.55 ± 0.52 mV) tended to become positive in contrast with the Zeta potential of PMS, indicating the encapsulation of IDA within the PDA-coated PVA microspheres.

Subsequently, the morphology and microstructural characteristics on the surface of PDA-coated dual-effect PVA microspheres were evaluated by scanning electron microscopy (SEM). As shown in Fig. 2d, each group had a uniform spherical or ellipsoidal shape. The PVA microspheres exhibited a smooth external surface, while the PMS particles had a rough external surface with irregular, heterogeneous and gully-like structure. The microstructural characteristics on the surface of PTMS, PIMS and PTIMS were similar to PMS, with the presence of drug crystal particles. However, the presence of a substantial quantity of crystalline on this surface, attributed to the insolubility of TQR and the excellent adhesion properties of PDA. Simultaneously, this indicated that TQR was encapsulated within the PMS microspheres, which could be attributed to the adhesive properties of the catechol groups and amine ions present in PDA[38]. Particle size analysis (Fig. 2e) revealed that PVA microspheres were predominantly concentrated around 110 μm, whereas the other microspheres exhibited a concentration of approximately 140 μm. Then, the EDS elemental mapping (Fig. 2f, g) to analyze PTIMS was implemented. The presence of carbon (C), nitrogen (N), oxygen (O), and chlorine (Cl) was distinctly demonstrated. C and O were the main elements of PVA, while C, N and O were the main elements of PMS and TQR. Cl was the characteristic element of IDA. The EDS results indicated the presence of C (35.117%), N (7.641%), O (40.862%), Cl (16.380%) distributed on the surface of the PTIMS, providing further evidence for the successful envelope of PDA and effective loading of TQR and IDA. As shown in Supplementary Fig. 2, the increased surface roughness of the PDA-coated microspheres not only indicated the successful modification of the PDA surface but also suggested a potential enhancement in their embolization effect, which was because the greater roughness facilitated clot formation by red blood cells within embolized vessels. At the same time, upon examination of the microspheres depicted in Supplementary Fig. 3a, it was observed that the prepared microspheres remained well-dispersed in solution without exhibiting any signs of aggregation. In Supplementary Fig. 3b, PTIMS microspheres were uniformly dispersed within a mixed solution of saline and iohexol. As demonstrated in Supplementary Video, the prepared PTMS microspheres exhibited smooth passage through the catheter, thereby confirming their excellent catheter passability.

Photothermal conversion performance, drug loading behavior and drug release behavior

The introduction of PDA conferred the PVA microspheres with excellent performance of photothermal conversion. Taking into account the repetitive photothermal ablation effect of PTT on the tumor following TACE,

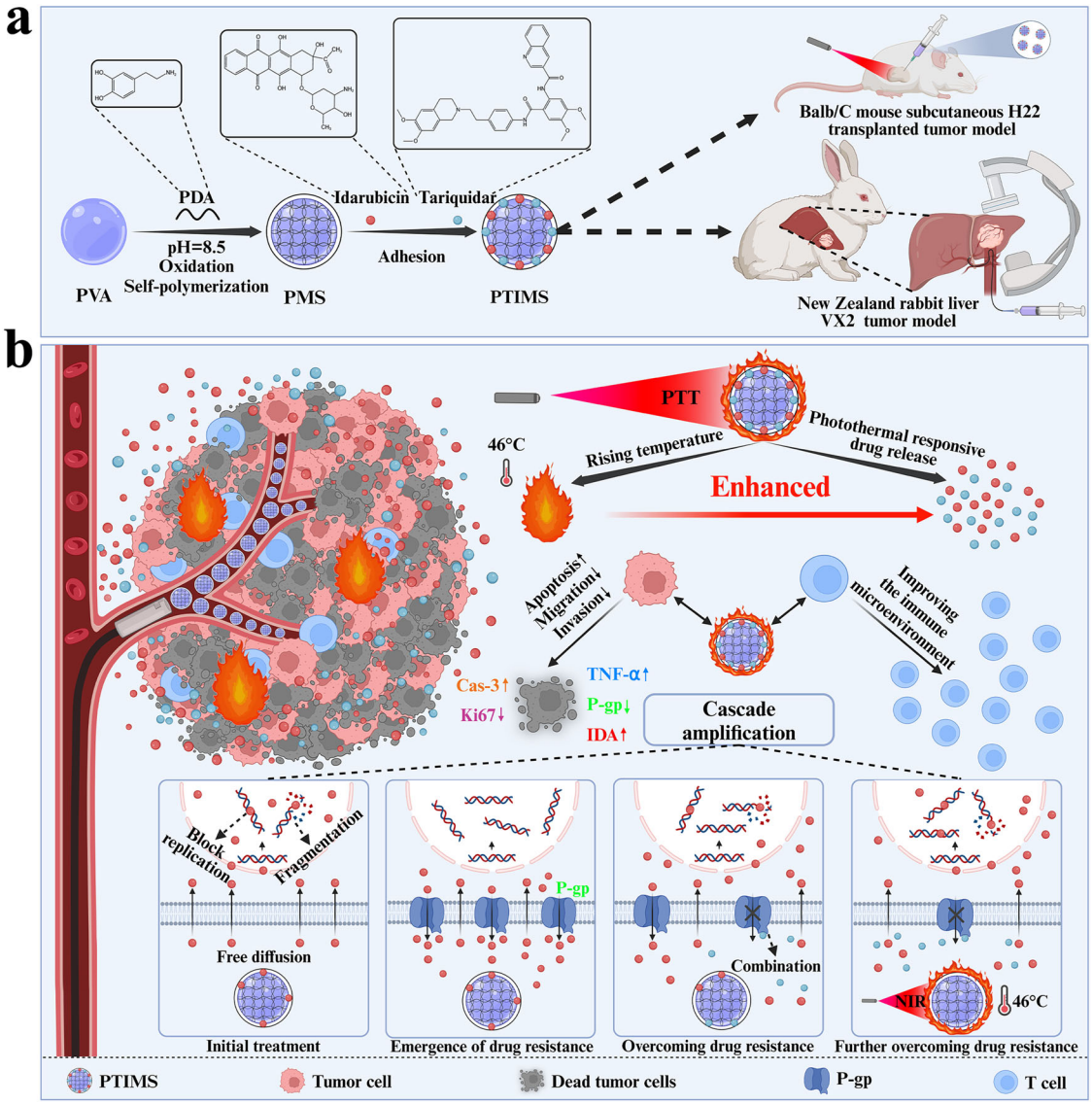

Fig. 1 | Schematic illustration of the dual-effect embolization microspheres loaded with IDA and TQR, in conjunction with PTT for HCC. a The preparation process of PTIMS and its application to the subcutaneous H22 transplanted tumor model in Balb/c mice and VX2 liver tumor model in New Zealand rabbits. **b** PTIMS in conjunction with PTT has been utilized to effectively address drug resistance and suppress the growth of HCC.

PVA, PMS, PTMS, PIMS and PTIMS were irradiated by 808 nm NIR with 0.5 and 0.8 W/cm^2 to evaluate the photothermal conversion performance, respectively. The real-time temperature was monitored, and the representative images were displayed in Fig. 3a. As shown in Fig. 3b, c, the temperature of PVA was elevated inconsiderably under NIR light irradiation at 27.77 ± 0.22 and 27.70 ± 0.05 °C, respectively. In contrast, the temperature of the remaining groups of samples increased continuously. At 0.5 W/cm^2, the temperature of PMS, PTMS, PIMS and PTIMS was elevated to 40.57 ± 0.49, 40.40 ± 0.43, 41.43 ± 0.62 and 41.23 ± 1.13 °C, while 46.13 ± 1.28, 46.33 ± 0.79, 45.87 ± 0.94 and 46.23 ± 0.90 °C at 0.8 W/cm^2. To achieve effective tumor inhibition by PTT (42–48 °C), the NIR power of 0.8 W/cm^2 was selected as the optimal choice for subsequent experiments. After undergoing five consecutive cycles of irradiation (Fig. 3d), the remarkable photothermal stability of PTIMS was demonstrated as evidenced by its ability to maintain a temperature rise up to 46.03 ± 0.74 °C. And the photothermal conversion efficiency (η) of PTIMS at 808 nm was 42.61%.

As shown in Fig. 3e, f, the drug loading behavior was evaluated. The entrapment rate of IDA was 65.39 ± 2.98% (PIMS) and 51.18 ± 2.92% (PTIMS). And the entrapment rate of TQR was 75.09 ± 1.39% (PTMS) and 63.17 ± 3.69% (PTIMS). The entrapment rate of samples from each group demonstrated that IDA and TQR could be loaded efficiently. The entrapment rate of PTIMS loaded with both drugs was slightly reduced; however, the entrapment rate for each drug remained above 50%. As shown in Supplementary Fig. 4, the drug loading capacity (DLC) of each microsphere group was systematically characterized. For single-drug systems, PIMS (IDA-only) and PTMS (TQR-only) exhibited DLC of 1.31 ± 0.06% and 1.50 ± 0.03%, respectively. In the dual-drug PTIMS, IDA and TQR DLC were 1.02 ± 0.06% and 1.26 ± 0.07%, showing a slight decrease. Despite this, PTIMS still maintained a drug loading rate of >1%. This value is comparable to that of clinically used drug-eluting microspheres (such as DC Beads with a drug loading rate of ~1–2%), proving that it has the drug-carrying capacity required for actual treatment. The reduction in dual-drug DLC is attributed to competitive adsorption on polydopamine coatings, low TQR solubility causing crystalline loss during washing, and molecular interactions (e.g., hydrogen bonding) hindering effective binding. Nevertheless, PTIMS maintains anti-tumor efficacy through synergistic drug action and photothermal-triggered release, balancing loading efficiency with therapeutic performance. The drug release behavior of PTIMS was evaluated (Fig. 3g, h). On the 28 days, the cumulative release rate of IDA was 75.51 ± 4.13% (PIMS), 69.74 ± 6.51% (PTIMS) and the cumulative release rate of TQR was

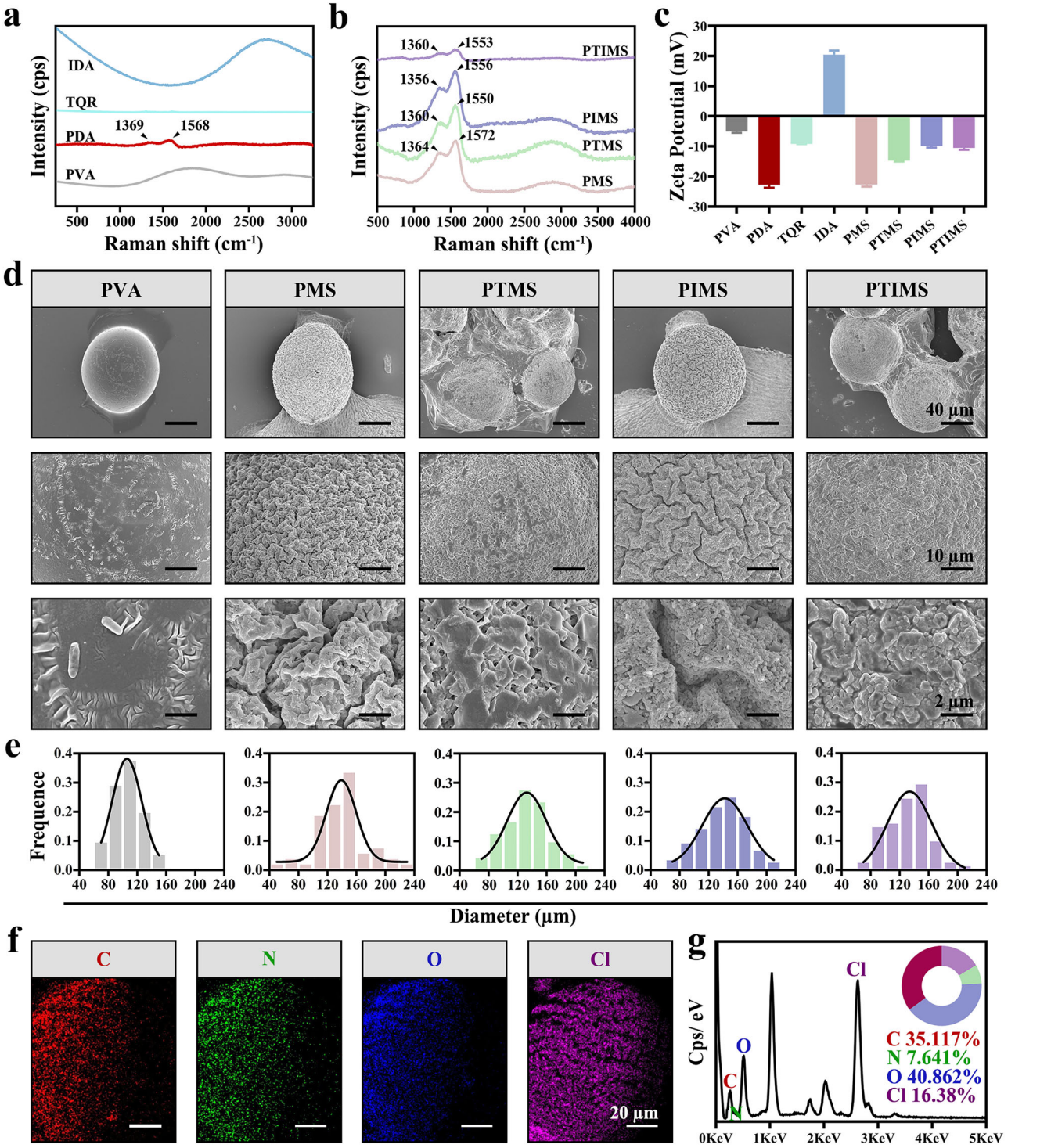

Fig. 2 | Physicochemical properties of PTIMS. a Raman spectra of PVA, PDA, TQR and IDA. **b** Raman spectra of PMS, PTMS, PIMS and PTIMS. **c** Zeta potential of each group. **d** Scanning electron microscopy (SEM) of microspheres at different magnifications. **e** Particle size analysis of microspheres. **f** and **g** SEM-energy dispersive spectrum (EDS) elemental mapping results of PTIMS. Scale bar: 2, 10, 20 and 40 μm. All error bars are the standard deviation.

84.73 ± 2.72% (PTMS) and 78.39 ± 1.87% (PTIMS). The drug release capability of PTIMS was consistent, as observed in the study conducted by K. Wu et al., aligning with the pharmacological requirements of microspheres for clinical treatment due to their high drug adsorption capacity and complete drug release[11,25]. To evaluate the photothermal-responsive drug release ability of PIMS and PTIMS, the release of IDA and TQR was examined under intermittent NIR with 0.8 W/cm^2. Under the NIR, the cumulative release rate of IDA was 92.08 ± 3.60% (PIMS + NIR) and 90.37 ± 3.24% (PTIMS + NIR) and the cumulative release rate of TQR was 94.16 ± 3.14% (PTMS + NIR) and 91.91 ± 3.23% (PTIMS + NIR), indicating that the photothermal conversion of PDA promoted the release of the drug.

Anti-tumor effect in vitro

Considering the excellent photothermal conversion performance of PTIMS and the photothermal responsive release of TQR and IDA, the synergistic anti-tumor effect of chemotherapy drugs in combination with PTT was

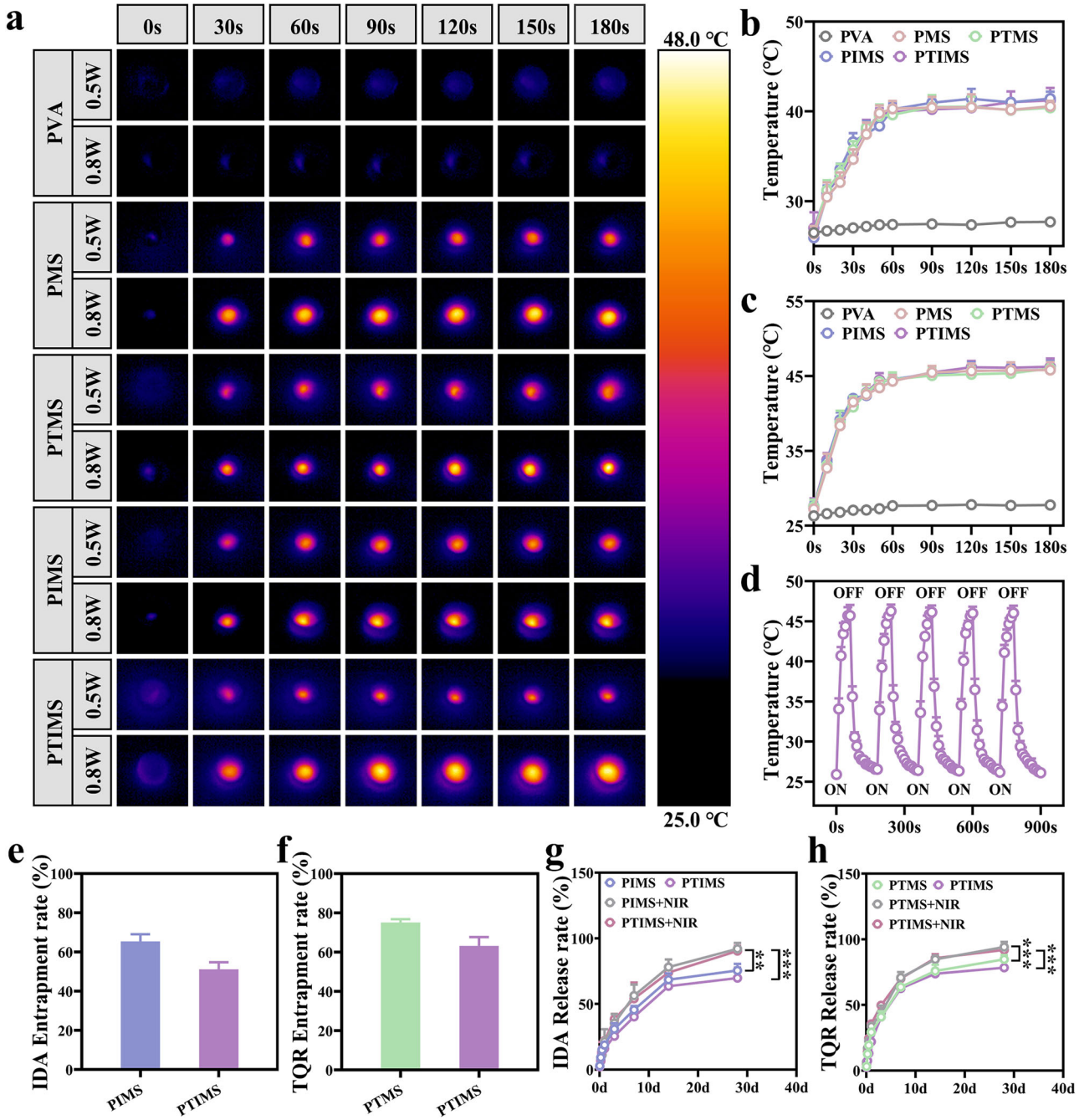

Fig. 3 | Photothermal and release behavior property of PTIMS. a Infrared thermal images of PVA, PMS, PTMS, PIMS, and PTIMS under 808 nm laser irradiation (0.5 and 0.8 W/cm^2) at 0, 30, 60, 90, 120, 150 and 180 s, respectively. **b** and **c** Temperature elevation curve for each group. **d** Temperature change of PTIMS during five on/ off cycles at 0.8 W/cm^2 irradiation. **e** and **f** Entrapment rate of PIMS, PTMS and PTIMS. **g** and **h** Drug releasing of PTIMS at room temperature and intermittent 0.8 W/cm^2 irradiation. All error bars are the standard deviation.

evaluated using H22 cells in vitro. As shown in Fig. 4a, PTIMS can promote apoptosis and inhibit the migration and invasion of tumor cells by raising the temperature and photothermal-responsive drug release. The results of the live and dead cell staining assay (Fig. 4b, c) showed no red dead cells in the B.C. and PTMS, with the respective percentages of 99.61 ± 0.55% and 99.80 ± 0.28% for live cells. In contrast, the red dead cells appeared in PIMS, PTIMS, PIMS + NIR and PTIMS + NIR with the respective percentage of 82.80 ± 6.26%, 67.89 ± 5.74%, 63.32 ± 3.37%, and 42.34 ± 3.29% for live cells, suggesting that the apoptotic effects of IDA were potentiated by TQR and further amplified under NIR, whereas TQR itself possessed no apoptotic effect. Cell Counting Kit-8 (CCK-8) assay (Fig. 4d) revealed that PIMS, PTIMS, PIMS + NIR and PTIMS + NIR exhibited significant cytotoxicity at 2 days compared with B.C. and PTMS. Meanwhile, the cell viability exhibited a distinct time-dependent decrease, ultimately reaching 28.40 ± 4.64% (PIMS), 14.49 ± 2.44% (PTIMS), 15.19 ± 1.69% (PIMS + NIR) and 5.01 ± 0.90% (PTIMS + NIR) at 3 days. Subsequently, the findings from the apoptosis assay (Fig. 4g and Supplementary Fig. 5) were consistent with those from the live and dead cell staining assay, thereby providing further substantiation for the preceding conclusion. IDA-induced apoptosis in tumor cells might be attributed to the generation of free radicals following iron ion chelation, which could cause damage to DNA, proteins and cellular membrane structures[26]. The percentage of apoptotic tumor cells was significantly increased in the PTIMS group, whereas no such increase was observed in the PTMS group. This difference might be attributed to the

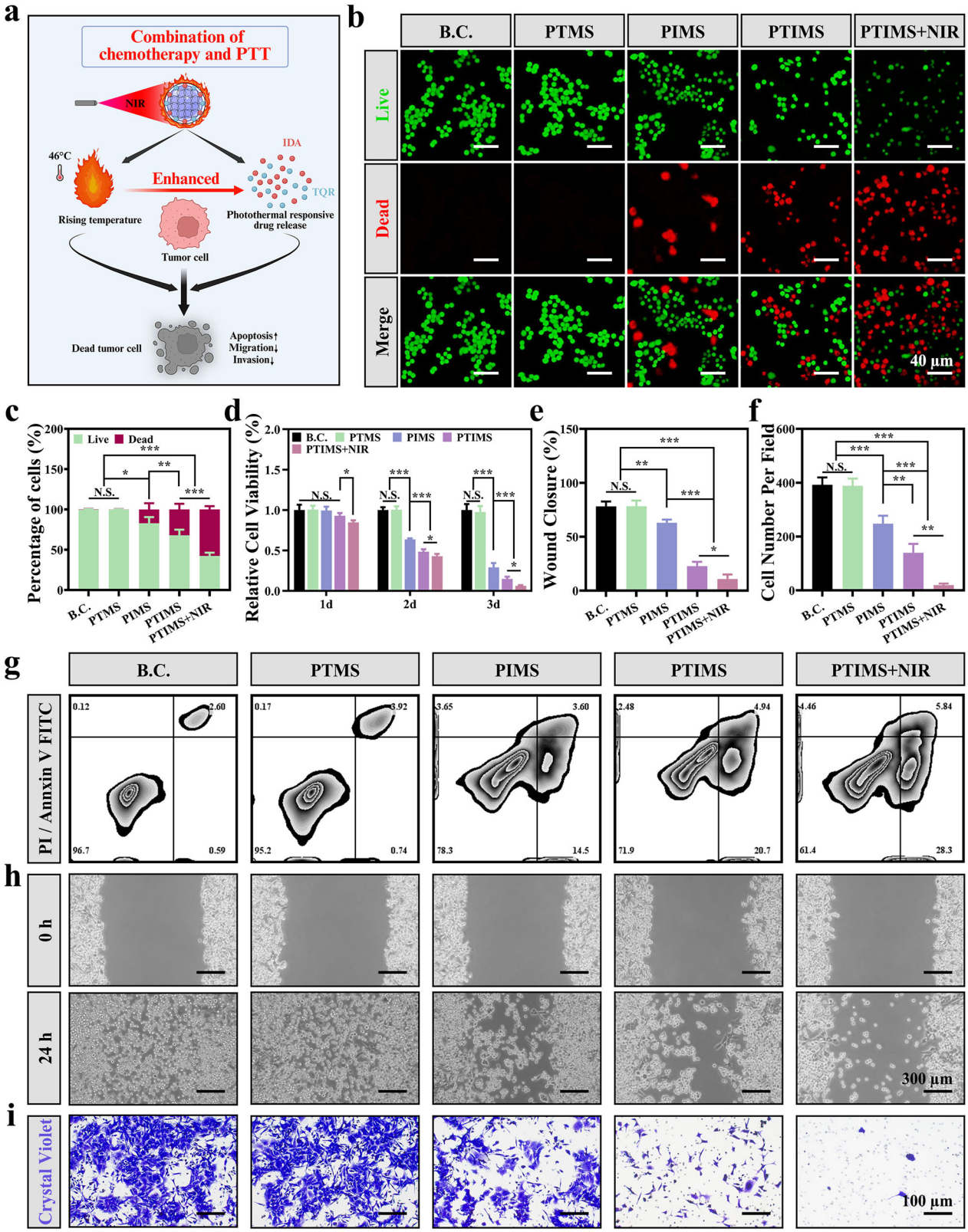

Fig. 4 | The anti-tumor effect of PTIMS + NIR in vitro. a Schematic illustration of anti-tumor mechanisms mediated by the combination of chemotherapy drugs and PTT. **b** Representative images of live and dead cell staining for H22 cells in different groups. **c** Percentage of live cells and dead cells in each group. **d** Relative cell viability of H22 cells co-cultured with each group at 1, 2, and 3 days, respectively. **e** and **f** Quantitative results of the scratch assay and Transwell assay. **g** Representative flow cytometry profiles (Annexin V-AbFluor™ 488/PI staining) in different groups. **h** and **i** Representative images of the scratch assay and Transwell assay. Scale bar: 40, 100, and 300 μm. Significant differences: N.S. no significant difference; $^{*}P < 0.05$; $^{**}P < 0.01$; $^{***}P < 0.001$. All error bars are the standard deviation.

inhibition of P-gp function or the reduction of P-gp expression in H22 cells following the addition of TQR. Simultaneously, the apoptotic effect was significantly enhanced in the PTIMS + NIR group, likely attributable to the pro-apoptotic impact of PTT on tumor cells and its role in enhancing chemosensitivity.

The high invasiveness and metastatic potential of hepatocellular carcinoma (HCC) represent one of the critical factors contributing to treatment failure. Therefore, inhibiting tumor cell migration and invasion is a pivotal strategy to enhance the efficacy of TACE. Therefore, the Scratch assay and Transwell assay were employed to systematically evaluate the impact of PTIMS + NIR on the migration and invasion capabilities of H22 cells. As shown in Fig. 4e and h, the migratory area decreased from 78.14 ± 3.70% (B.C.) and 78.27 ± 4.32% (PTMS) to 62.88 ± 2.46% (PIMS), 22.73 ± 3.27% (PTIMS), 40.98 ± 2.75% (PIMS + NIR) and 10.76 ± 3.41% (PTIMS). Similarly, the number of invasive cells (Fig. 4f and i) was from 392.00 ± 22.38 in B.C. and 388.33 ± 21.85 in PTMS to 247.67 ± 24.14 in PIMS, 139.67 ± 26.89 in PTIMS, 134.00 ± 8.98 in PIMS + NIR and 19.33 ± 4.64 in PTIMS + NIR. Notably, TQR alone (PTMS) showed no inhibitory effect on migration and invasion, confirming its role as a P-gp inhibitor rather than a direct cytostatic agent. In contrast, the combination of IDA + TQR in PTIMS significantly enhanced the inhibition, which was further amplified by the NIR-induced photothermal effect. These results emphasize the dual mechanism of PTIMS + NIR—chemotherapy-induced cytostasis and photothermal-enhanced drug retention through P-gp suppression—in preventing HCC migration and invasion, thereby addressing a key mechanism of treatment resistance and metastatic spread.

Next, the anti-proliferative ability was assessed using the Ki67 immunofluorescence staining. As shown in Fig. 5a, b, the mean fluorescence intensity (MFI) of Ki67 decreased from 100.00 ± 7.17% in B.C. and 99.08 ± 5.78% in PTMS to 76.06 ± 6.29% in PIMS, 52.55 ± 6.07% in PTIMS, 59.86 ± 4.06% in PTIMS and 28.63 ± 4.17% in PTIMS + NIR. Subsequently, in order to quantitatively assess the cellular uptake of IDA, we conducted spectral analysis to determine its absorption and emission spectra, as well as identified the excitation wavelength (485 nm) and emission wavelength (551 nm) specific to IDA (Supplementary Fig. 6a, b). The quantification of IDA uptake was performed using flow cytometry due to the close excitation and emission wavelengths of IDA with the PE channel. A significant increase in IDA uptake was observed in the PTIMS, PIMS + NIR and PTIMS + NIR groups (Fig. 5c, d). Therefore, we hypothesized that the addition of TQR could reduce the expression of P-gp, curtail the active efflux of IDA from tumor cells and augment the intracellular concentration of IDA. Additionally, a further augmentation of this effect under PTT was observed, which could be attributed to the heightened chemosensitivity of tumor cells induced by PTT.

Ultimately, the molecular mechanism was investigated through immunofluorescence staining of P-gp and IDA. As shown in Fig. 5e–g, the MFI of P-gp was 100.00 ± 4.40% in B.C., 21.92 ± 2.89% in PTMS, 54.33 ± 3.89% in PIMS, 15.88 ± 2.38% in PTIMS, 16.55 ± 0.51% in PIMS + NIR and 5.06 ± 1.46% in PTIMS + NIR. The expression of P-gp was decreased after adding TQR, and further decreased in PTIMS + NIR group. And the MFI of IDA was 37.23 ± 3.89% in PIMS, 67.29 ± 7.48% in PTIMS, 52.76 ± 3.66% in PIMS + NIR and 100 ± 7.50% in PTIMS + NIR, demonstrating a significant enhancement in the cellular uptake of IDA upon the addition of TQR, which was further augmented under PTT. Additionally, the impact of PTIMS + NIR on P-gp expression was validated through Western blot experiments (Supplementary Fig. 7). The PTIMS + NIR group exhibited a reduction in P-gp expression. In conclusion, our findings indicated that the incorporation of TQR led to a reduction in P-gp expression in tumor cells, and PPT further diminished P-gp expression levels, consequently enhancing IDA uptake. To further validate the synergistic interaction between PTIMS and NIR, we employed the Bliss independence model to quantitatively assess the synergistic effect (Supplementary Fig. 8)[39]. The calculated R_2 (0.83 ± 0.01) value was lower than R_1 (0.99 ± 0.0007), suggesting that PTIMS and NIR exerted a synergistic effect in inducing tumor cell death.

Effect of PTIMS+NIR on subcutaneous H22 transplanted tumors in mice

Based on the aforementioned in vitro findings, a subcutaneously transplanted tumor model using mouse H22 cells was established. Local administration of PTIMS and PTT was subsequently employed to further assess their anti-tumor efficacy, photothermal characteristics and the mechanism underlying the reversal of tumor drug resistance. The in vivo photothermal conversion performance of PTIMS injected into the tumor was assessed through irradiation with NIR at 0.8 W/cm^2. In Fig. 6a, b, the local temperature of the PTIMS was rapidly heating up to 46.17 ± 1.3 °C, thereby demonstrating the excellent in vivo photothermal conversion performance of the PTIMS, and the photothermal conversion efficiency was 30.34%. In Fig. 6d and Supplementary Fig. 9, compared with B.C. (1079.18 ± 50.44 mm^3) and PTMS (968.49 ± 53.27 mm^3), the tumor volume of PIMS (675.21 ± 50.20 mm^3), PTIMS (321.43 ± 58.09 mm^3), PIMS + NIR (383.77 ± 73.44 mm^3), and PTIMS + NIR (110.08 ± 49.33 mm^3) was significantly reduced, and the growth of tumor volume in PTIMS + NIR was the most observably inhibited. At the same time, we observed that the tumor volume in the PTIMS + NIR group was significantly smaller than that in the B.C. group on day 4. A statistically significant difference was noted between the groups, suggesting that the drug release rate on day 4 (TQR was 54.65 ± 1.23% and IDA was 42.81 ± 2.12%) may represent the minimum effective level required for tumor suppression by PTIMS + NIR. Then, histological evaluation of the isolated tumor tissue was performed. As depicted in Fig. 6g, the tumor sections of the PTIMS + NIR treatment group presented a significantly higher occurrence of karyolysis and karyopyknosis, along with a more marked degree of cell necrosis compared to the hematoxylin and eosin (H&E) staining outcomes of the other groups. As shown in Fig. 6c, e and h, the positive TNF-α stained area was 6.42 ± 0.77% in B.C., 9.39 ± 0.94% in PTMS, 18.60 ± 1.32% in PIMS, 32.81 ± 3.09% in PTIMS, 28.43 ± 1.59% in PIMS + NIR and 46.00 ± 2.28% in PTIMS + NIR, and the number of Ki67$^+$ cells/mm^2 was 4437 ± 313 in B.C. and 3901 ± 383 in PTMS, 2596 ± 101 in PIMS, 1793 ± 90 in PTIMS, 1604 ± 146 in PIMS + NIR and 833 ± 61 in PTIMS + NIR. Subsequently, the P-gp immunofluorescence staining (Fig. 6i) showed that the expression level of P-gp was decreased from 100 ± 4.52% in B.C., 82.24 ± 4.97% in PIMS, 20.03 ± 1.84% in PTMS, 52.88 ± 4.82% in PIMS + NIR, 20.40 ± 3.62% in PTIMS and 6.90 ± 1.49% in PTIMS + NIR. The aforementioned findings collectively indicate that the growth of tumors was significantly inhibited by PTIMS + NIR, potentially attributing to the inhibition of P-gp by TQR and the augmentation of tumor eradication and chemosensitivity by NIR. Additionally, given the paramount importance of biosafety in the in vivo application of biomaterials, organ tissue samples (heart, liver, spleen, lung and kidney) and fresh plasma from each group were collected for subsequent histological and biochemical analyses. The H&E staining (Supplementary Fig. 10) results revealed no discernible variations in multiple organs between the B.C. group and the other experimental groups and the biochemical indicators including alanine transaminase (ALT), aspartate transaminase (AST), alkaline phosphatase (ALP), blood urea nitrogen (BUN), creatinine (CREA) and uric acid (UA) were within the standard range as well (Supplementary Fig. 11).

PTIMS inhibiting VX2 liver tumors in New Zealand rabbits

The efficacy of PTIMS in TACE was further investigated based on the aforementioned ideal in vitro and in vivo experimental results. Initially, the microspheres should be delivered into the hepatic artery via the microcatheter and brought into direct contact with the blood, necessitating caution to prevent unnecessary iatrogenic hemolysis. Therefore, the results of the hemolysis assay were shown in Fig. 7c. The hemolysis rate (HR) of PIMS, PTMS and PTIMS was below 5% ($P < 0.05$), which exhibited a comparable level to that of the commercially available microsphere PVA, indicating the absence of any significant hemolysis. Subsequently, as shown in Fig. 7a and Supplementary Fig. 12, enhanced CT at 0 days revealed significant arterial phase enhancement along the tumor periphery, accompanied by areas of low-density liquefaction and necrosis within, thereby confirming the

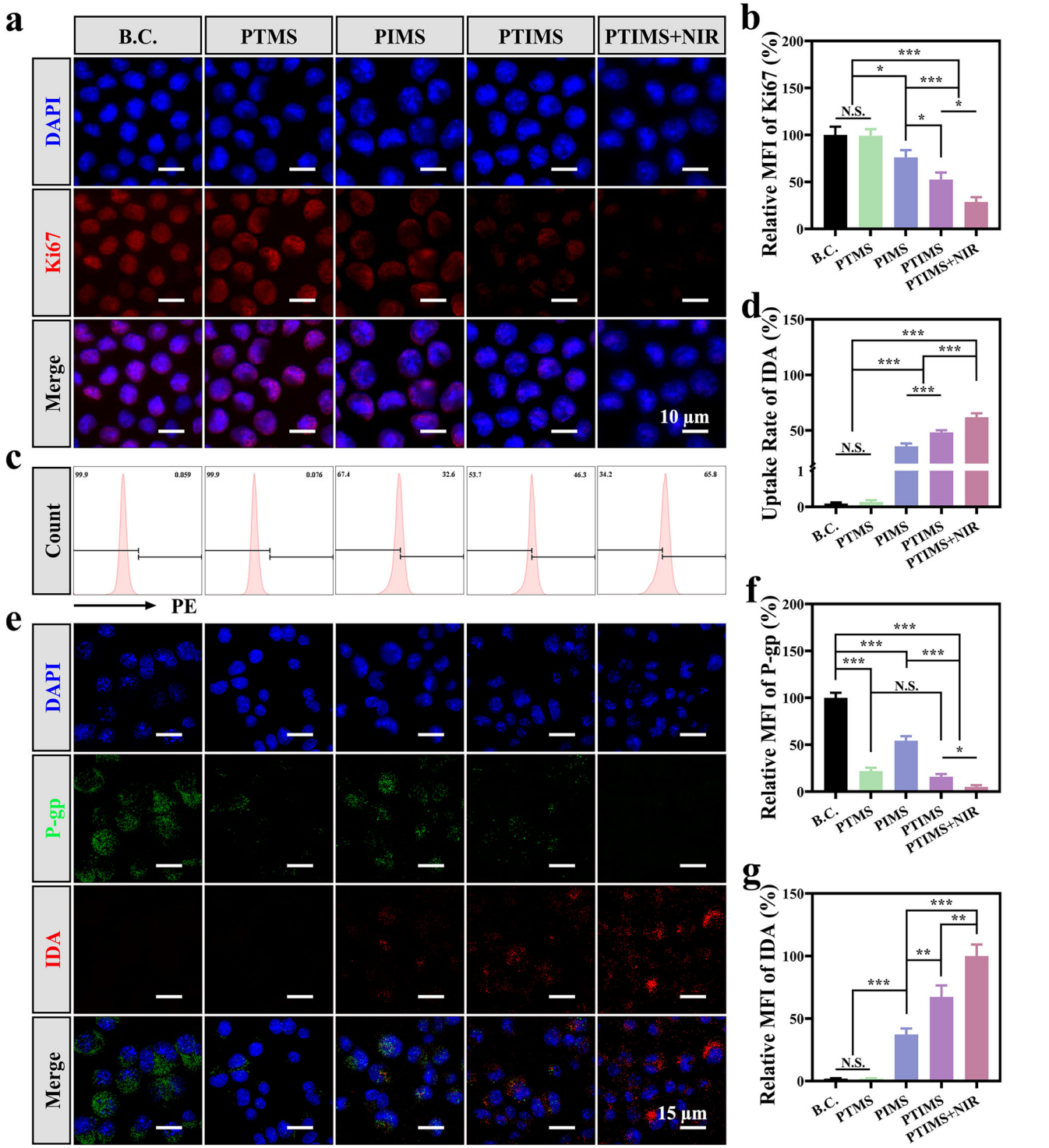

Fig. 5 | The mechanism of the anti-tumor effect of PTIMS + NIR in vitro. a and **b** Representative images and statistical analysis of Ki67 immunofluorescence staining. **c** and **d** Flow cytometry and statistical analysis of the IDA uptake. **e–g** Representative images and statistical analysis of P-gp and IDA immunofluorescence staining. Scale bar: 10 and 15 μm. Significant differences: N.S. no significant difference; $^{*}P < 0.05$; $^{**}P < 0.01$; $^{***}P < 0.001$. All error bars are the standard deviation.

successful establishment of VX2 liver tumors in New Zealand rabbits. Then, the tumor was subjected to TACE guided by DSA (Fig. 7b). The preoperative angiography demonstrated dense vascular distribution around VX2 liver tumors located in the left lobe of the liver, and the postoperative angiography demonstrated complete embolization of the vessels surrounding the tumor. Finally, the enhanced CT imaging (Fig. 7a and Supplementary Fig. 12) revealed no significant high-density enhancement areas in the PTIMS group following TACE treatment, whereas residual tumor tissue was still observed in the PVA group. Additionally, the tumor volume in the PTIMS group was notably smaller compared to that in the PVA group, indicating that PTIMS not only effectively embolizes tumor blood vessels but also exerts an anti-tumor effect through the release of IDA and TQR.

To further evaluate the embolization effect of PTIMS, histological analysis was performed. As shown in Supplementary Fig. 13 and Fig. 7d, the

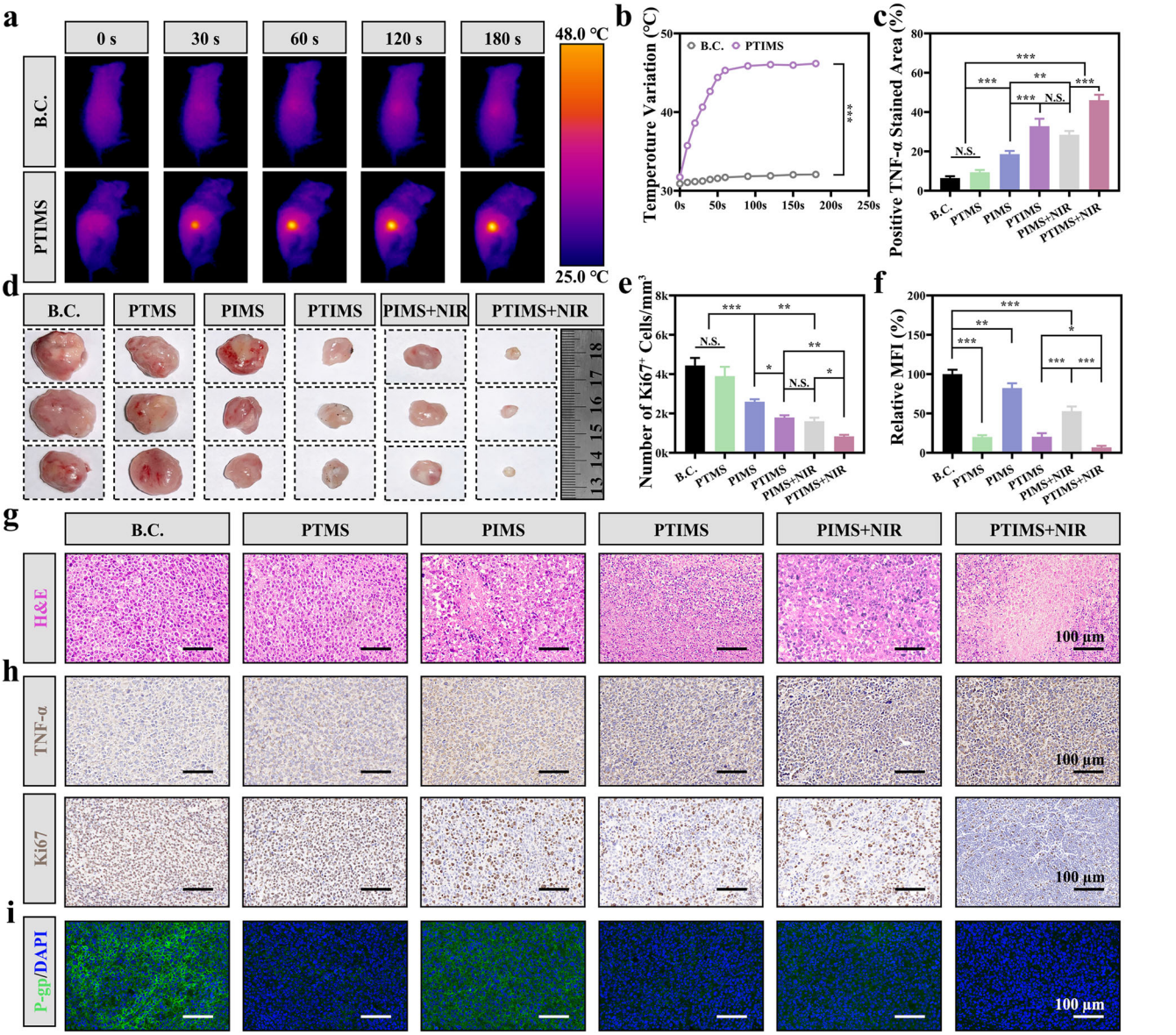

Fig. 6 | Effect of PTIMS + NIR on subcutaneous H22 transplanted tumors in mice. a and **b** Representative images and statistical analysis of photothermal performance in vivo. **c** Statistical analysis of TNF-α immunohistochemical staining. **d** Representative images of tumors in each group two weeks after treatment. **e** and **f** Statistical analysis of Ki67 immunohistochemical staining and P-gp immunofluorescence staining. **g–i** Representative images of H&E staining, TNF-α and Ki67 immunohistochemical staining and P-gp immunofluorescence staining. Scale bar: 100 μm. Significant differences: N.S. no significant difference; $^{*}P < 0.05$; $^{**}P < 0.01$; $^{***}P < 0.001$. All error bars are the standard deviation.

microspheres were not found in B.C., while the brown-black PDA-coated microspheres were present in PTMS, PIMS and PTIMS, indicating that the vessels of VX2 liver tumors were successfully embolized after TACE. Subsequently, the immunohistochemical staining (Fig. 7e, h and i) results showed the number of $Ki67^{+}$ cells/mm^2 was 312 ± 26 in B.C., 297 ± 22 in PTMS, 220 ± 10 in PIMS and 117 ± 7 in PTIMS, while the positive area of Cas-3 was 15.39 ± 0.80% in B.C., 18.58 ± 2.18% in PTMS, 34.80 ± 1.71% in PIMS and 57.91 ± 1.28% in PTIMS. Ultimately, the expression of P-gp and the immune microenvironment in tumor tissues was evaluated through immunofluorescence staining. As shown in Fig. 7f and j, the relative MFI of P-gp was 100.00 ± 6.37% in B.C., 1.87 ± 0.37% in PTMS, 84.13 ± 5.77% in PIMS and 1.16 ± 0.45% in PTIMS. The findings suggested that TQR enhanced the anti-proliferative and pro-apoptotic effects of IDA, potentially through its ability to inhibit the expression of P-gp, which leads to a reduction in IDA efflux and an increase in IDA accumulation within tumor cells. As shown in Fig. 7g and k, the relative MFI of CD8 was 100.00 ± 26.98% in PVA, 213.96 ± 31.09% in PTMS, 335.09 ± 38.97% in PIMS and 505.72 ± 36.15% in PTIMS. By using scRNA sequencing and functional assay, Jizhou Tan et al. discovered that both the number and function of $CD8^{+}$ T cells were compromised in post-TACE HCC, which was consistent with the results of PVA group[40]. In the PTIMS group, $CD8^{+}$ T cells were significantly increased, consistent with the findings of Zhiying Zheng et al.[8].

Additionally, considering the significance of biological safety as a pivotal parameter in the advancement of novel medical devices, the pathological alterations of heart, spleen, lung and kidney and the biochemical indicators including ALT, AST, BUN and CREA were evaluated. As shown in Supplementary Figs. 14 and 15, the HE staining of each group revealed no evident pathological alterations, and the biochemical indicators of each group remained within the normal range on both 0 and 14 days.

Discussion

During the TACE treatment process, tumor resistance to various chemotherapeutic agents has increasingly garnered attention[40]. According to

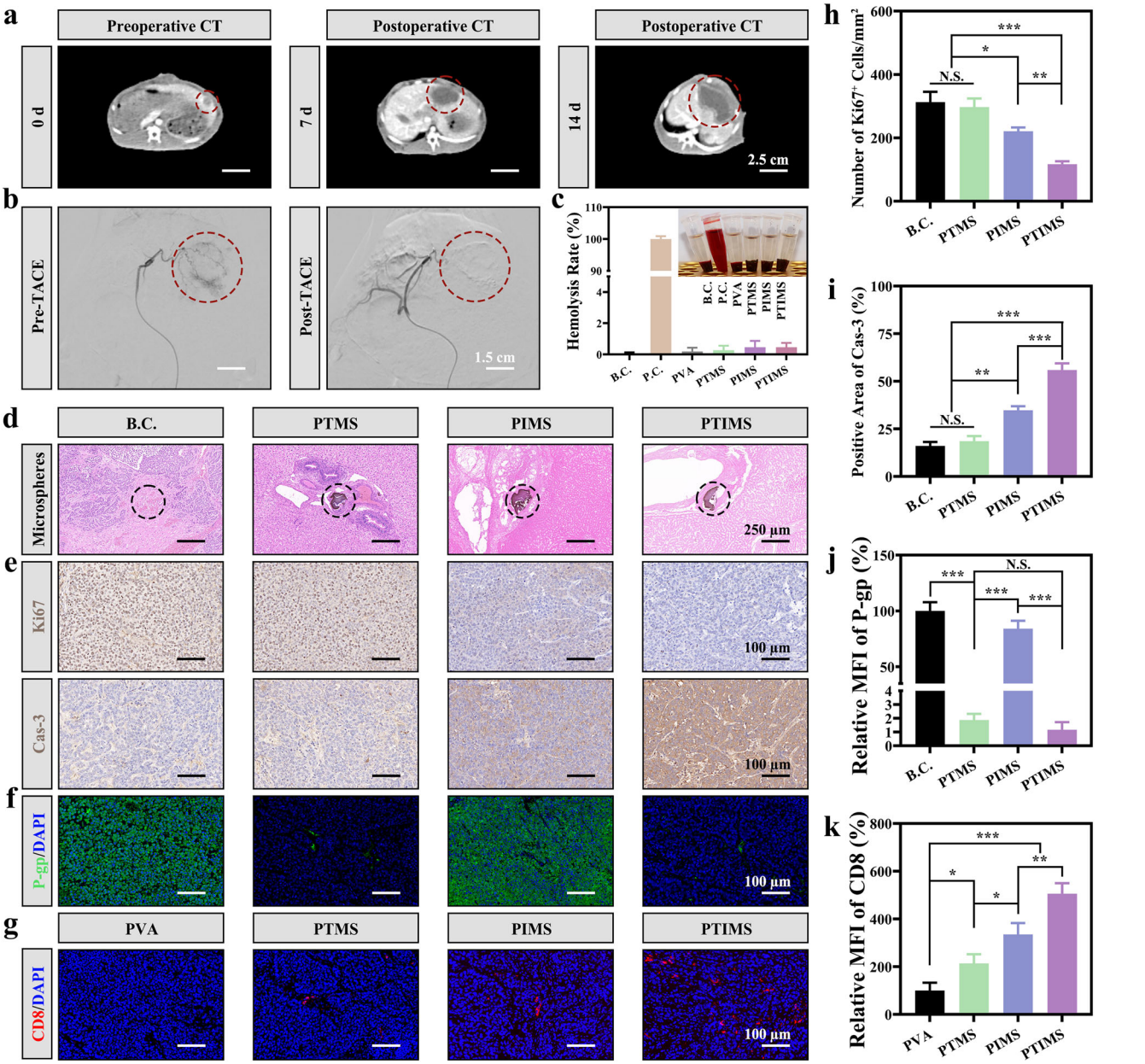

Fig. 7 | PTIMS inhibiting VX2 liver tumors in New Zealand rabbits. **a** Representative images enhanced CT scan at 0, 7, and 14 days after the embolization of PTIMS. **b** The DSA images of pre-TACE and post-TACE. **c** Hemolysis rate of red blood cells. **d** The H&E staining images of embolic tissues. **e** and **f** Representative images of Ki67 and Cas-3 immunohistochemical staining and P-gp immunofluorescence staining. **g** Representative images of CD8 immunofluorescence staining. **h**–**k** Statistical analysis of Ki67 and Cas-3 immunohistochemical staining and P-gp and CD8 immunofluorescence staining. Scale bar: 2.5, 1.5 cm, 250 and 100 μm. Significant differences: N.S. no significant difference; $^{*}P < 0.05$; $^{**}P < 0.01$; $^{***}P < 0.001$. All error bars are the standard deviation.

the study by S.T. Tia et al.[41], MDR is closely associated with P-gp expressed on the cell membrane. In parallel, photothermal functional biomaterials have attracted growing interest in the field[42]. J. Zhou et al. reported a strategy involving transcatheter arterial infusion of Bi–Ln nanoparticles combined with PTT for the treatment of HCC[43]. As a minimally invasive strategy for photothermal ablation following TACE, PTT has demonstrated promising potential in preventing tumor recurrence and enabling minimally invasive applications. However, there have been limited studies combining P-gp inhibitors, TACE, and PTT. Presently, most ongoing studies focus on developing microspheres to integrate TACE with thermotherapy[44,45]. Challenges such as uncontrolled temperature, side effects from sudden drug release, and tumor multidrug resistance continue to impede progress in this field. In this study, PDA-coated PTIMS loaded with IDA and TQR were employed to elevate the local tumor temperature under NIR irradiation, enabling controlled and sustained drug release, thereby enhancing anti-tumor efficacy. IDA primarily exerts cytotoxic effects, while TQR demonstrates the capacity to overcome multidrug resistance by down-regulating the expression of P-gp on the tumor cell membrane.

In addition, the combined application of drugs and hyperthermia in the present study demonstrated synergistic effects, rather than merely additive ones. Although existing studies have provided evidence supporting the synergistic interaction between drugs and hyperthermia, few have explored the underlying mechanisms. The study by C. Wei et al. [46] and K. Fang et al. [47] confirmed the synergistic tumor-killing effect by evaluating the impact of drugs and hyperthermia on tumor cell viability. However, it did not further elucidate the intrinsic mechanism—namely, that hyperthermia enhances tumor cell sensitivity to the administered drugs.

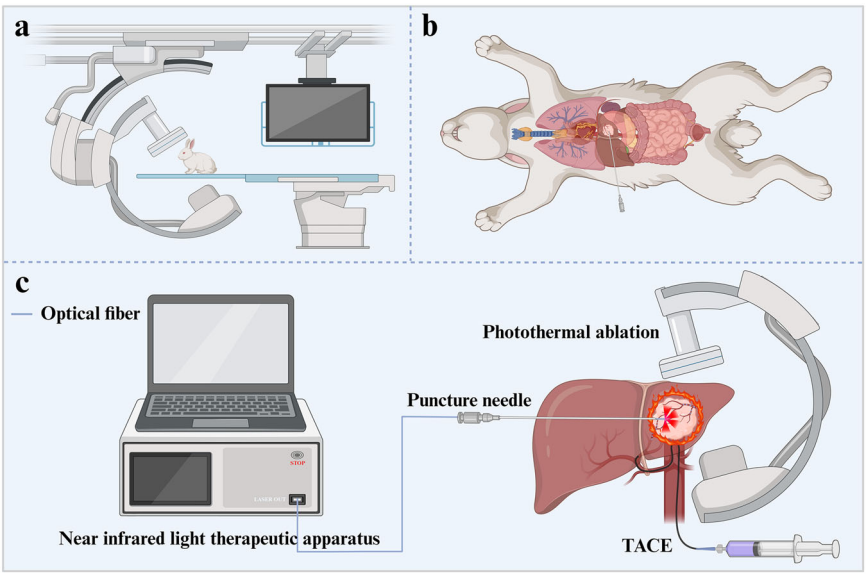

Fig. 8 | Schematic illustration of photothermal ablation therapy after TACE treatment in the New Zealand rabbit VX2 liver tumor model. a New Zealand rabbits were anesthetized and placed on a DSA apparatus. **b** The puncture needle reaching the tumor site. **c** Following TACE, PTIMS in conjunction with PTT was utilized for the treatment of VX2 tumors.

Compared with the emulsion containing a single chemotherapeutic agent typically employed in c-TACE and the drug-loaded microspheres utilized in DEB-TACE, the combination regimen of PTIMS and NIR can effectively prevent the early, rapid release of drugs during chemotherapy. Even the more stable L-Arg@CaPL emulsion developed by D. Wang et al.[48] and the ICN-LPE emulsion developed by XC. Xia et al.[49] exhibited cumulative drug release rates exceeding 60% after 80 and 48 h, respectively. The CMs microspheres developed by JX. Huang et al.[50] exhibited a more pronounced initial burst release during the early stage. In contrast, in this study, the cumulative drug release from PTIMS + NIR after three days remained below 50%. Additionally, the 3Asphere microspheres developed by J. Guo et al., although capable of preventing abrupt drug release, do not achieve complete drug release[51]. For instance, only ~50% of the drug was released into PBS over a period of 28 days, whereas PTIMS + NIR achieved a release rate exceeding 90% within the same timeframe. Furthermore, the controlled release mechanism exhibited by PTIMS, which combines baseline sustained release with photothermal triggering, demonstrates greater precision compared to those employed in current studies of single-response systems (e.g., magnetothermal systems[52]), making it suitable for multi-stage treatment of drug-resistant tumors. Additionally, while TARE eradicates tumors through localized radiation, it carries risks of radiation exposure and potential extrahepatic organ damage (such as radiation pneumonitis[53]). In contrast, the PTIMS + NIR approach eliminates the need for radiation and effectively circumvents radiation-related adverse effects.

Moreover, Erick L. Bastos et al. reported a penetration depth of near-infrared light in skin tissue of 800 μm[54], which poses a significant challenge for achieving effective photothermal ablation of VX2 liver tumors in New Zealand rabbits. Consequently, in the next phase (Fig. 8), we intend to collaborate with the Laser Manufacturing Institute of Henan Academy of Sciences to design an integrated puncture photothermal ablation system[43]. The specific plan is summarized as follows: (1) Intraoperative stage: Only fiber optic implantation is performed, without light and heat irradiation, reducing the operation time. (2) Postoperative stage: Photothermal therapy can be performed at the bedside or in an outpatient setting 24 h after surgery, activated by a portable near-infrared (NIR) device. This percutaneous approach to delivering photothermal therapy to deep tumors may hold significant promise for consolidative treatment following TACE in hepatocellular carcinoma. It is believed that through the unremitting efforts of scientists, engineers, doctors, enterprises and others, it can be expected to achieve clinical transformation and benefit mankind.

Conclusion

The dual-effect microspheres loaded with IDA and TQR were developed for use in TACE combined with minimally invasive photothermal therapy. As a clinically validated chemotherapeutic agent in TACE, IDA exerts potent anti-tumor effects, while TQR, acting as a P-gp inhibitor, suppresses P-gp expression on tumor cell membranes, thereby blocking the IDA efflux and overcoming MDR in tumors. PDA, renowned for its excellent biocompatibility, demonstrates remarkable photothermal conversion ability and stability, serving as an ideal heat source for photothermal ablation therapy. The PTIMS serves as a drug carrier, exhibiting temperature-responsive drug release. Collectively, PTIMS effectively overcomes tumor MDR and exhibits superior therapeutic efficacy in preclinical models, highlighting its substantial potential for clinical translation in HCC treatment. This integrated strategy of combining chemotherapy, MDR reversal, and photothermal ablation via PTIMS represents a promising advancement in TACE-based cancer therapy.

Methods

Preparation of PTIMS

Tris–HCl buffer (pH = 8.8) was used to prepare a 0.2% dopamine solution. After that, 2 g of 8 Spheres (named PVA) were added to a solution immersed in 50 mL of 0.2% dopamine. After stirring at room temperature for 48 h, the microspheres were washed with deionized water to remove unreacted dopamine, and then allowed to stand for 10 min to collect the precipitate, which was PDA-coated PVA microspheres (named PMS).

TQR and IDA solutions were prepared by dissolving 10 mg of TQR powder and 10 mg of IDA powder in 10 mL of PBS buffer, followed by thorough mixing and shaking. The blend solution of TQR solution and IDA was obtained by mixing 10 mg of TQR powder and 10 mg of IDA powder together in 10 mL of PBS buffer. Then, 0.5 g of PMS was added to each of the above three solutions and incubated for 24 h on a shaker, followed by centrifugation at 3000 rpm for 5 min. Finally, TQR microspheres (named PTMS), IDA microspheres (named PIMS) and TQR/IDA microspheres (named PTIMS) were obtained.

Physicochemical properties of PTIMS

Bond vibrations were tested by Raman spectroscopy (Thermo Scientific DXR 3Xi, USA) at 0 to 6000 cm^{-1}. Zeta potential was measured with a Nano-2S90 Zeta Sizer (Malvern Instruments, UK). Optical microscopy was employed to examine the morphology of the prepared microspheres. SEM images and EDS dispersion maps of the tested samples were obtained using a JSM-7401F microscope (JEOL, Japan) equipped with an EDS system, and

then the surface morphology and elemental composition of the samples were analyzed. Fifty microspheres for each group were selected from the SEM images, and the size distribution was counted using the ImageJ software. And the morphology of PVA, PMS, PTMS, PIMS and PTIMS was observed using an atomic force microscope (AFM, Dimension 3100, Veeco, USA).

The catheter passability of PTIMS was also assessed. Specifically, PTIMS were suspended at optimal concentrations in a saline–iohexol mixture (with a 1:1 ratio of saline to iohexol) and subsequently injected through a 2.7 F catheter. The process was recorded on video.

In vitro photothermal properties of PTIMS

To evaluate the photothermal performance, 0.2 g of each sample (2 g/mL) was irradiated with 808 nm NIR for 180 s, and the power was set to 0.5 and 0.8 W/cm^2, respectively. The thermography was obtained using an infrared thermal imaging camera (Testo, Shanghai, China), and the temperature changes of each sample were recorded in real time. In addition, the PTIMS was subjected to five cycles of laser irradiation heating (808 nm, 0.8 W/cm^2) and natural cooling to evaluate its photothermal stability. The photothermal conversion efficiency (η) of PTIMS at 808 nm, 0.8 W/cm^2 NIR irradiation was calculated using the following formula:

$$\eta = \frac{hA(\Delta T_1 - \Delta T_2)}{I(1 - 10^{-A808})} \quad (1)$$

where h is the heat transfer coefficient, A is the surface are of the container, ΔT_1 is the temperature change of PTIMS, ΔT_2 is the temperature change of solvent, I is the laser power and A808 is the absorbance of PTIMS at 808 nm.

In vitro drug loading behavior and drug release behavior of PTIMS

The concentration of IDA was determined by measuring the absorbance of each solution at 484 nm with a UV spectrophotometer[55]. The quantification of TQR was performed via high-performance liquid chromatography (HPLC). A Mightysil C18 RP18 column (5 μm, 4.6 × 250 nm, Kanto Chemical. Co. Inc., Tokyo, Japan) was employed for the separation at 35 °C. The mobile phases consist of (A) 10 mM ammonium acetate buffer (pH = 5), (B) acetonitrile and (C) methanol. The injection volume of each solution was 40 μL and the flow rate was 1 mL/min. For TQR analysis, the mobile phases ratio was A:B:C = 53:42:5(v/v/v) and UV detection was 254 nm[56,57].

Accurately weigh 10 mg of TQR and 10 mg of IDA separately, and transfer each into a 10 mL volumetric flask. The volume was adjusted to the mark with PBS buffer solution and thoroughly mixed to obtain 1 mg/mL solutions of TQR and IDA, respectively. Different volumes of solutions were aspirated by pipette and placed in 10 mL volumetric flasks to prepare solutions with concentrations of 2, 5, 10, 20, 100 and 500 μg/mL. A standard curve was established after detection using the above methods.

Drug loading behavior of PTIMS

The supernatant in 2.2 was collected, and the IDA and TQR contents in the supernatant were determined using the method described above to calculate the entrapment rate (ER) and the drug loading capacity (DLC).

$$ER = \frac{X_0 - X_1}{X_0} \times 100\% \quad (2)$$

where X_0 was the initial drug loading amount and X_1 was the drug loading amount of supernatant.

$$DLC = \frac{\text{Mass of the drug encapsulation}}{\text{Mass of drug eluting microspheres}} \times 100\% \quad (3)$$

Drug release behavior of PTIMS

Drug release was performed by placing 0.2 g of PTMS, 0.2 g of PIMS, 0.2 g of PTIMS, and 0.2 g of PTIMS in 10 mL PBS buffer, respectively. The temperature of the fixed constant temperature oscillator was 37 °C and the speed was 50 r/min. PIMS and PTIMS were irradiated with 808 nm laser at 0.8 W/cm^2 for 5 min every 2 days to study the effect of photothermal on drug release. Samples were taken at 1, 6, 12 h, 1, 3, 7, 14 and 28 days, and the same volume of corresponding PBS buffer was added to each sample. The drug content in each sample was detected as described above, and the cumulative drug release rate was calculated. The drug concentration of PTIMS combined with NIR was determined on the fourth day, based on the changes in tumor volume observed in the in vivo experiment.

In vitro anti-tumor effects of PTIMS

H22 cells were used to verify the anti-tumor effects. This study was divided into six groups, named B.C. (an equal volume of PBS buffer was added), PTMS, PIMS, PTIMS, PIMS + NIR and PTIMS + NIR, respectively. Samples from PTMS, PIMS and PTIMS were immersed in PBS buffer for 24 h. The samples from PIMS + NIR and PTIMS + NIR were immersed in PBS buffer for 24 h, and the samples were irradiated using NIR (808 nm, 0.8 W/cm^2) for 5 min every 2 h. The supernatants were collected after centrifugation for further use. In the PIMS + NIR and PTIMS + NIR groups, the supernatant was added and then treated with a water bath at 45 °C for 5 min to simulate the photothermal environment.

CCK-8 assay

The effect of PTIMS on the relative cell viability (%) of H22 cells was evaluated by CCK-8 assay, as described in previous studies[58]. Specifically, digested H22 cells (3×10^3 cells per well) were seeded in 96-well plates and cultured at 37 °C in 5% CO_2. After that, the cells were treated with the extracts of each group and incubated for 1, 2, and 3 days. After adding 10% CCK-8 solution to each well, the cells were incubated at 37 °C for 2 h and detected by a microplate reader at 450 nm.

$$\text{Relative cell viability}\,(\%) = \frac{OD_1 - OD_3}{OD_2 - OD_3} \times 100\% \quad (4)$$

where OD_1 was the OD value of PTMS, PIMS, PTIMS, PIMS + NIR and PTIMS + NIR, respectively, OD_2 was the OD value of B.C., and OD_3 was the OD value of blank character (no cells, only medium and 10% CCK-8 solution).

Live and dead cells staining

Digested H22 cells (1×10^5 cells per well) were seeded in 24-well plates and cultured at 37 °C in 5% CO_2. The cells were then treated with the extracts of each group and incubated for 24 h. The cells were stained with the live and dead cell double staining kit (KTA1001) and then observed by inverted fluorescence microscopy.

Apoptosis assay

Digested H22 cells (2×10^5 cells per well) were seeded in six-well plates and cultured at 37 °C in 5% CO_2. After that, the cells were treated with the extracts of each group and incubated for 24 h. They were washed with PBS buffer, digested to single cell suspensions, stained with Annexin V-AbFluorTM488 and PI and then detected by flow cytometry (NOVOCYte3130, ACEA, America).

Scratch assay

Digested H22 cells (2×10^5 cells per well) were seeded in six-well plates and cultured at 37 °C in 5% CO_2. After overnight culture (cell confluence reached more than 90%), the cells were strewed using a 10 μL sterile pipetting tip and washed away with PBS buffer to remove free cells. Subsequently, the cells were treated with the extracts of each group and photographed under a light microscope at 0 and 24 h, respectively. Wound healing rate = $(W_1 - W_2)/W_0 \times 100\%$. W_1 is the scratch area at 0 h; W_2 is the scratch area at 24 h.

Transwell assay

H22 cells (2×10^4 cells per chamber) treated with the extracts of each group were seeded into the upper chamber. After co-incubation with cultures at 37 °C and 5% CO_2 for 48 h, non-migrating cells retained on the upper surface of the filter membrane were removed with a cotton swab. Migrating cells on the lower surface of the filter membrane were fixed using 4% paraformaldehyde and subsequently stained with 0.5% crystal violet solution for 30 min and photographed under a light microscope.

Immunofluorescence staining

For analysis of Ki67 and P-gp expression in H22 cells, H22 cells were incubated on cover slides and treated with extracts from each group for 24 h, followed by fixation with 4% paraformaldehyde and treatment with 0.1% Triton-100. They were then treated with goat serum for 30 min at 25 °C. H22 cells were incubated with primary antibodies against Ki67 and P-gp, and all groups were incubated with FITC and Cy3-labeled secondary antibodies (Supplementary Tables 1 and 2). Nuclei were stained with DAPI.

To examine the cellular uptake of IDA, data acquisition was performed using a confocal laser scanning microscope (CLSM, Zeiss LSM 800, Germany) at Ex.534 nm/Em.572 nm.

Cellular uptake assay of IDA

To examine cellular uptake of IDA, we first examined the excitation (from 350 to 650 nm) and emission spectra (from 500 to 800 nm) of IDA using the UV spectrophotometer (CURY5000, Agilent) and the fluorescence spectrometer (F7000, Hitachi)[59], respectively. Then, digested H22 cells (1×10^5/mL) were seeded in six-well plates and cultured at 37 °C in 5% CO_2. After that, the cells were treated with the extracts of each group and incubated for 24 h. They were washed with PBS buffer, digested to single cell suspensions and detected by flow cytometry (NOVOCYte3130, ACEA, America).

Western Blotting

H22 cells (1×10^5/mL) were inoculated in 6-well plates and incubated with B.C. and PTIMS + NIR for 24 h. The treated H22 cells were collected and lysed with RIPA. The proteins were isolated by sodium dodecyl sulfate (SDS) and sodium dodecyl sulfate-polyacrylamide gel electrophoresis (SDS–PAGE), and transferred to nitrocellulose membranes. Next, the membranes were sealed with 5% milk for 1 h, and the primary antibody was incubated overnight at 4 °C. The secondary antibody was added and incubated for 1 h. Subsequently, the high-efficiency chemiluminescence detection reagent was added to the mixture for 5 min. Bands of P-gp and Actin on the membranes were detected by a chemiluminescence instant aging system (Supplementary Tables 1 and 2).

Synergistic effect of PTIMS and NIR

The synergistic effect of PTIMS and NIR was evaluated using the CCK-8 assay at 24 h. This study was divided into four groups, named B.C., PTIMS, NIR (treated with a water bath at 45 °C for 5 min to simulate the photothermal environment) and PTIMS + NIR, respectively. We subsequently evaluated the effects of PTIMS and NIR by the formulation of the Bliss independent model.

$$R_1 = R_{PTIMS} + R_{NIR} - R_{PTIMS} \times R_{NIR} \quad (5)$$

where R_1 was the relative cell viability (%) in anticipation of additive effects, R_{PTIMS} and R_{NIR} were the relative cell viability (%) of PTIMS and NIR, and R_2 was the relative cell viability (%) of actual combined effects.

Effect of PTIMS on subcutaneous H22 transplanted tumors in mice

Direct intratumoral injection was used in mice to ensure uniform drug distribution and minimize variability in vascular perfusion, which is a preliminary step before optimizing TACE protocols in larger animals. To evaluate the effect of PTIMS in inhibiting H22 tumor growth in vivo, female Balb/C mice (6 weeks of age) were purchased from the Laboratory Animal Center of Hualan Biological Co., Ltd for follow-up studies. All animals were bred in the Animal Experiment Center of Henan Province (SPF sterile grade). Mice were randomly divided into six groups of B.C. (injection of an equal volume of PBS buffer), PTMS, PIMS, PTIMS, PIMS + NIR and PTIMS + NIR (NIR radiation at 0.8 W/cm^2 for 5 min every 2 days after injection of PTIMS into the tumor).

Construction of the Balb/C mouse subcutaneous H22 transplanted tumor model

150 μL of PBS buffer containing 1×10^7 resuspended H22 cells was injected into the right antero-dorsal side of Balb/C mice. When the tumor size reached 100 mm^3, 0.2 g of samples from each group was injected into the tumor of each mouse, which was recorded as 0 days. Tumor volume was measured every 2 days. All implantation procedures were approved by the Animal Care Committee of the First Affiliated Hospital of Zhengzhou University and complied with the National Institutes of Health Guidelines for the Care and Use of Laboratory Animals.

In vivo photothermal performance

Based on the results of in vitro photothermal performance tests, NIR at 0.8 W/cm^2 was selected for in vivo evaluation. At the first NIR treatment after sample injection, mice in the B.C. and PTIMS + NIR groups were NIR irradiated to evaluate the photothermal performance of PTIMS + NIR. Data on temperature changes were recorded in the same manner as before.

Histological analysis and biochemical analysis

At 14 days, after mice were euthanized, tumor tissues were collected, fixed in 4% paraformaldehyde, embedded in paraffin and sectioned. H&E staining, immunofluorescence staining (labeled as P-gp) and immunohistochemical staining (labeled as Ki67 and TNF-α) were subsequently performed according to the corresponding standard procedures (Supplementary Tables 1 and 2). The histological changes were observed under a microscope. In addition, the heart, liver, spleen, lung, and kidney of mice in each group were collected for H&E staining and serum samples of mice were collected to detect ALT, AST, ALP, BUN, CREA and UA. ALT, AST, ALP, BUN, CREA and UA were detected by an automatic biochemical analyzer (Chemray 800, Rayto), and the wavelength was set as 340, 340, 405, 340, 546, and 510 nm.

PTIMS inhibiting VX2 liver tumors in New Zealand rabbits

Construction of rabbit VX2 liver tumor model. Twenty New Zealand male rabbits were purchased from Hualan Biological Co., Ltd. and randomly divided into four groups. The groups were B.C., PTMS, PIMS and PTIMS. All experimental animals were anesthetized via injection of sodium pentobarbital. Following anesthesia, the animals were positioned in the supine position, and the subxiphoid region was prepared and sterilized according to aseptic techniques. The skin was incised along the midline of the abdomen to expose the liver. VX2 tumor tissue (purchased from the company Rochen Pharma) was excised into 1 mm^3 fragments and subsequently implanted into the left lobe of the liver using a 21 G needle. Hemostasis was achieved by applying a medical gelatin sponge to the wound site. The muscle and skin layers were closed with sutures and further sterilized. Postoperatively, antibiotics were administered for three consecutive days, and the animals were housed in the SPF environment. All procedures were approved by the Animal Care Committee of the First Affiliated Hospital of Zhengzhou University (ZZU-LA20210423[02]) and complied with the National Institutes of Health Guidelines for the Care and Use of Laboratory Animals.

Hemolysis evaluation. The hemolytic potential of each group of microspheres was assessed using the methodology described in our previous study[60,61]. The groups were B.C. (normal saline), PC (pure water), PVA, PTMS, PIMS, and PTIMS. Specifically, whole blood was taken from the rabbit heart and diluted with normal saline at a ratio of 1:1.25. The B.C. (normal saline), PC (pure water), PVA, PTMS, PIMS and

PTIMS were co-incubated with the diluted blood for 1 h at 37 °C. After that, they were centrifuged at 3000 rpm for 10 min to observe the hemolysis state. The absorbance value of the supernatant at 545 nm was detected by a microplate analyzer (BioTek, USA). Hemolysis ratio (HR) was calculated using the following formula:

$$HR = \frac{AS - AN}{AP - AN} \times 100\% \quad (6)$$

where AS, AP, and AN represent the average absorbance values of the samples, the positive control, and the negative control, respectively.

TACE. Two weeks after implantation in the liver of experimental rabbits, enhanced CT was used to evaluate whether the growth of VX2 liver tumor tissue met the tumor formation criteria (labeled as 0 days), including the location and size of VX2 liver tumors. When the tumor met the specified criteria, transcatheter arterial chemoembolization was performed under digital subtraction angiography (DSA). In brief, a 2 cm incision was made in the right groin of the experimental rabbit and the femoral artery was exposed. A 5-F catheter was inserted into the femoral artery, followed by a 2.7-F microcatheter and 0.021-inch guidewire. The microcatheter was moved to the tumor-feeding artery, and the tumor was embolized according to group assignment. Re-angiography after treatment confirmed that the tumor-feeding artery was completely embolized. After that, the microcatheter, guidewire and catheter were removed, and the femoral artery was sutured. All animals were injected with antibiotics for 3 days after surgery. Enhanced CT scan was performed on rabbits in PVA and PTIMS at 7 and 14 days after TACE to evaluate the embolization effect. The tumor volume was calculated on CT images:

$$V = \frac{ab^2}{2}$$

where a is the longest diameter line measured and b is the shortest diameter line perpendicular to it.

Histological analysis and biochemical analysis. At 14 days after TACE, after euthanizing the experimental rabbits, tumor tissues were collected, fixed in 4% paraformaldehyde, embedded in paraffin and sectioned. H&E staining, immunofluorescence staining (labeled as P-gp and CD8) and immunohistochemical staining (labeled as Ki67 and Cas-3) were subsequently performed according to the corresponding standard procedures (Supplementary Tables 1 and 2). The histological changes were observed under a microscope. In addition, the heart, spleen, lung and kidney of experimental rabbits in each group were collected for H&E staining, and the serum samples of experimental rabbits were collected to detect ALT, AST, BUN and CREA. ALT, AST, ALP, BUN, CREA and UA were detected by an automatic biochemical analyzer (Chemray 800, Rayto), and the wavelength was set as 340, 340, 405, 340, 546 and 510 nm.

The integrated puncture photothermal ablation system. As illustrated in Fig. 8, we first identified the tumor location post-TACE under DSA fluoroscopy (Fig. 8a), followed by puncturing the designated site with a puncture needle (Fig. 8b, Supplementary Fig. 16). After removing the needle core, we inserted the optical fiber from the external laser transmitter (Supplementary Fig. 17) into the puncture site to reach the tumor location. Finally, we adjusted the parameters of the laser transmitter to achieve photothermal ablation of hepatocellular carcinoma following TACE.

Statistical analysis

Results are expressed as means ± SD and Student's t-test was used for two-group comparisons and one-way ANOVA or two-way ANOVA was utilized for multiple comparisons. All statistical analyses were performed using GraphPad Prism 8.0 and presented as $P < 0.05$ to determine whether there was a significant difference (N.S. no significant difference; $^{*}P < 0.05$; $^{**}P < 0.01$; $^{***}P < 0.001$).

Data availability

The data that support the findings of this study are available from the corresponding author upon reasonable request.

Received: 18 February 2025; Accepted: 14 October 2025;
Published online: 25 November 2025

References

1. Yang, J. D. et al. A global view of hepatocellular carcinoma: trends, risk, prevention and management. *Nat. Rev. Gastroenterol. Hepatol.* **16**, 589–604 (2019).
2. Llovet, J. M. et al. Hepatocellular carcinoma. *Nat. Rev. Dis. Prim.* **7**, 6 (2021).
3. Reig, M. et al. BCLC strategy for prognosis prediction and treatment recommendation: the 2022 update. *J. Hepatol.* **76**, 681–693 (2022).
4. Sieghart, W., Hucke, F. & Peck-Radosavljevic, M. Transarterial chemoembolization: modalities, indication, and patient selection. *J. Hepatol.* **62**, 1187–1195 (2015).
5. Hu, J. et al. Advances in biomaterials and technologies for vascular embolization. *Adv. Mater.* **31**, e1901071 (2019).
6. Liu, L. et al. Magnetic mesoporous embolic microspheres in transcatheter arterial chemoembolization for liver cancer. *Acta Biomater.* **130**, 374–384 (2021).
7. Du, L. et al. Synthesis and assessment of drug-eluting microspheres for transcatheter arterial chemoembolization. *Acta Biomater.* **88**, 370–382 (2019).
8. Zheng, Z. et al. Idarubicin-loaded biodegradable microspheres enhance sensitivity to anti-PD1 immunotherapy in transcatheter arterial chemoembolization of hepatocellular carcinoma. *Acta Biomater.* **157**, 337–351 (2023).
9. Wang, D. & Rao, W. Bench-to-bedside development of multifunctional flexible embolic agents. *Theranostics* **13**, 2114–2139 (2023).
10. Poon, R. T. et al. A phase I/II trial of chemoembolization for hepatocellular carcinoma using a novel intra-arterial drug-eluting bead. *Clin. Gastroenterol. Hepatol.* **5**, 1100–1108 (2007).
11. Wu, K. et al. Celecoxib and cisplatin dual-loaded microspheres synergistically enhance the trans-arterial chemoembolization effect of hepatocellular carcinoma. *Mater. Today Bio* **24**, 100927 (2024).
12. Liu, Y., Bhattarai, P., Dai, Z. & Chen, X. Photothermal therapy and photoacoustic imaging via nanotheranostics in fighting cancer. *Chem. Soc. Rev.* **48**, 2053–2108 (2019).
13. Silva, F. et al. 2D Nanomaterials and their drug conjugates for phototherapy and magnetic hyperthermia therapy of cancer and infections. *Small* **20**, e2306137 (2024).
14. Guo, R. et al. Engineered nanomaterials for synergistic photo-immunotherapy. *Biomaterials* **282**, 121425 (2022).
15. Liu, S., Pan, X. & Liu, H. Two-dimensional nanomaterials for photothermal therapy. *Angew. Chem. Int. Ed. Engl.* **59**, 5890–5900 (2020).
16. Wang, Y., Zhang, X. & Yue, H. Two-dimensional nanomaterials induced nano-bio interfacial effects and biomedical applications in cancer treatment. *J. Nanobiotechnol.* **22**, 67 (2024).
17. Wu, M. et al. Polydopamine-coated radiolabeled microspheres for combinatorial radioembolization and photothermal cancer therapy. *ACS Appl. Mater. Interfaces* **15**, 12669–12677 (2023).
18. Zhang, Y. et al. Study of a multiple responses, high deformation, and programmable PLA-PPC/PVA-PDA actuator. *Macromol. Rapid Commun.* **44**, e2300327 (2023).

19. Xiong, Y., Rao, Y., Hu, J., Luo, Z. & Chen, C. Nanoparticle-based photothermal therapy for breast cancer noninvasive treatment. *Adv. Mater.* **37**, e2305140 (2023).
20. Overchuk, M., Weersink, R. A., Wilson, B. C. & Zheng, G. Photodynamic and photothermal therapies: synergy opportunities for nanomedicine. *ACS Nano* **17**, 7979–8003 (2023).
21. Chen, M. et al. Homogenous multifunctional microspheres induce ferroptosis to promote the anti-hepatocarcinoma effect of chemoembolization. *J. Nanobiotechnol.* **20**, 179 (2022).
22. Wu, S. et al. Smart nanoparticles and microbeads for interventional embolization therapy of liver cancer: state of the art. *J. Nanobiotechnol.* **21**, 42 (2023).
23. Ma, P. & Mumper, R. J. Anthracycline nano-delivery systems to overcome multiple drug resistance: a comprehensive review. *Nano Today* **8**, 313–331 (2013).
24. Gaba, R. C., Emmadi, R., Parvinian, A. & Casadaban, L. C. Correlation of doxorubicin delivery and tumor necrosis after drug-eluting bead transarterial chemoembolization of rabbit VX2 liver tumors. *Radiology* **280**, 752–761 (2016).
25. Guiu, B. et al. Idarubicin-loaded beads for chemoembolization of hepatocellular carcinoma: the IDASPHERE II Single-Arm Phase II Trial. *Radiology* **291**, 801–808 (2019).
26. Minotti, G., Menna, P., Salvatorelli, E., Cairo, G. & Gianni, L. Anthracyclines: molecular advances and pharmacologic developments in antitumor activity and cardiotoxicity. *Pharm. Rev.* **56**, 185–229 (2004).
27. Garg, A. D. et al. Trial watch: Immunogenic cell death induction by anticancer chemotherapeutics. *Oncoimmunology* **6**, e1386829 (2017).
28. Sivak, L. et al. Overcoming multidrug resistance via simultaneous delivery of cytostatic drug and P-glycoprotein inhibitor to cancer cells by HPMA copolymer conjugate. *Biomaterials* **115**, 65–80 (2017).
29. Yuan, G. et al. Multifunctional nanoplatforms application in the transcatheter chemoembolization against hepatocellular carcinoma. *J. Nanobiotechnol.* **21**, 68 (2023).
30. Dong, J., Yuan, L., Hu, C., Cheng, X. & Qin, J. J. Strategies to overcome cancer multidrug resistance (MDR) through targeting P-glycoprotein (ABCB1): An updated review. *Pharm. Ther.* **249**, 108488 (2023).
31. Zhang, L., Ye, B., Chen, Z. & Chen, Z. S. Progress in the studies on the molecular mechanisms associated with multidrug resistance in cancers. *Acta Pharm. Sin. B* **13**, 982–997 (2023).
32. Chen, D. Q. et al. The role of ABCC10/MRP7 in anti-cancer drug resistance and beyond. *Drug Resist. Updat.* **73**, 101062 (2024).
33. Li, X. Q. et al. Reversal of P-gp and BCRP-mediated MDR by tariquidar derivatives. *Eur. J. Med. Chem.* **101**, 560–572 (2015).
34. Braconi, L. et al. Tetrazole and oxadiazole derivatives as bioisosteres of tariquidar and elacridar: new potent P-gp modulators acting as MDR reversers. *Eur. J. Med. Chem.* **259**, 115716 (2023).
35. Pan, Y. et al. Novel dendritic polyglycerol-conjugated, mesoporous silica-based targeting nanocarriers for co-delivery of doxorubicin and tariquidar to overcome multidrug resistance in breast cancer stem cells. *J. Control. Release* **330**, 1106–1117 (2021).
36. Yakdoumi, F. Z., Hadj-Hamou, A. S., Rahoui, N., Rahman, M. M. & Abetz, V. Polylactic acid nanocomposites containing functionalized multiwalled carbon nanotubes as antimicrobial packaging materials. *Int. J. Biol. Macromol.* **213**, 55–69 (2022).
37. Damberga, D. et al. Influence of PDA coating on the structural, optical and surface properties of ZnO nanostructures. *Nanomaterials* **10**, https://doi.org/10.3390/nano10122438 (2020).
38. Xie, X. et al. Intervention of polydopamine assembly and adhesion on nanoscale interfaces: state-of-the-art designs and biomedical applications. *Adv. Healthc. Mater.* **10**, e2002138 (2021).
39. Ma, J. & Motsinger-Reif, A. Current methods for quantifying drug synergism. *Proteom. Bioinform.* **1**, 43–48 (2019).
40. Tan, J. et al. TREM2(+) macrophages suppress CD8(+) T-cell infiltration after transarterial chemoembolisation in hepatocellular carcinoma. *J. Hepatol.* **79**, 126–140 (2023).
41. Tia, S. T., Luo, M. & Fan, W. Mapping the role of P-gp in multidrug resistance: insights from recent structural studies. *Int. J. Mol. Sci.* **26**, https://doi.org/10.3390/ijms26094179 (2025).
42. Lee, T., Kim, K. S. & Na, K. Nanocracker capable of simultaneously reversing both P-glycoprotein and tumor microenvironment. *J. Control. Release* **354**, 268–278 (2023).
43. Zhou, J. et al. Transcatheter intra-arterial infusion combined with interventional photothermal therapy for the treatment of hepatocellular carcinoma. *Int J. Nanomed.* **15**, 1373–1385 (2020).
44. Yang, H. et al. Self-delivery photothermal-boosted-nanobike multi-overcoming immune escape by photothermal/chemical/immune synergistic therapy against HCC. *J. Nanobiotechnol.* **22**, 137 (2024).
45. Yang, N. et al. Liquid metal microspheres with an eddy-thermal effect for magnetic hyperthermia-enhanced cancer embolization-immunotherapy. *Sci. Bull.* **68**, 1772–1783 (2023).
46. Wei, C. et al. CT/MR detectable magnetic microspheres for self-regulating temperature hyperthermia and transcatheter arterial chemoembolization. *Acta Biomater.* **153**, 453–464 (2022).
47. Fang, K. et al. Magnetic field activated drug release system based on magnetic PLGA microspheres for chemo-thermal therapy. *Colloids Surf. B Biointerfaces* **136**, 712–720 (2015).
48. Wang, D. et al. Arginine-loaded nano-calcium-phosphate-stabilized lipiodol pickering emulsions potentiates transarterial embolization-immunotherapy. *Adv. Sci.***12**, e2410484 (2025).
49. Xia, X. et al. A lipiodol pickering emulsion stabilized by iron-doped carbon nanozymes for liver transarterial chemoembolization. *Adv. Sci.* **12**, e2410873 (2025).
50. Huang, J. X. et al. Dual-drug loaded chondroitin sulfate embolization beads enhance TACE therapy for HCC by integrating embolization, chemotherapy, and anti-angiogenesis. *Mater. Today Bio* **30**, 101419 (2025).
51. Guo, J. et al. Tumor vessel-adaptable adhesive and absorbable microspheres for sustainable transarterial chemoembolization therapy. *Nat. Commun.* **16**, 6239 (2025).
52. Huang, J. X. et al. A study on overcoming post-TACE drug resistance in HCC based on controllable oxygen release-magnetic hyperthermia therapy. *Adv. Healthc. Mater.* **13**, e2402253 (2024).
53. Kim, H. C. Radioembolization for the treatment of hepatocellular carcinoma. *Clin. Mol. Hepatol.* **23**, 109–114 (2017).
54. Bastos, E. L., Quina, F. H. & Baptista, M. S. Endogenous photosensitizers in human skin. *Chem. Rev.* **123**, 9720–9785 (2023).
55. Gunduz, U. et al. Idarubicin-loaded folic acid conjugated magnetic nanoparticles as a targetable drug delivery system for breast cancer. *Biomed. Pharmacother.* **68**, 729–736 (2014).
56. Yu, C. P., Lin, S. W., Tsai, J. C. & Shyong, Y. J. Long acting tariquidar loaded stearic acid-modified hydroxyapatite enhances brain penetration and antitumor effect of temozolomide. *Eur. J. Pharm. Biopharm.* **197**, 114231 (2024).
57. Kim, C. H. et al. Functionalized lipid nanocarriers for simultaneous delivery of docetaxel and tariquidar to chemoresistant cancer cells. *Pharmaceuticals* **16**, https://doi.org/10.3390/ph16030349 (2023).
58. Zhao, Y. et al. In situ nanofiber patch boosts postoperative hepatocellular carcinoma immune activation by trimodal combination therapy. *ACS Nano* **18**, 245–263 (2024).
59. Wang, Y., Zhong, H., Yang, J., Yao, Y. & Li, L. Solvents/photo/pillar[5]arene triple responsive morphology and luminescence transformation from an amphiphilic dicyanostilbene-functionalized thiophene. *Chin. Chem. Lett.* **34**, 108452 (2023).
60. Zhao, Y. et al. All-in-one bioactive properties of photothermal nanofibers for accelerating diabetic wound healing. *Biomaterials* **295**, 122029 (2023).

61. Zhao, Y. et al. Construction of antibacterial photothermal PCL/AgNPs/BP nanofibers for infected wound healing. *Mater. Des.* **226**, 111670 (2023).

Acknowledgements

Thanks to Biorender for the resources. We thank Liufei Yang of the School of Fine Arts of Zhengzhou University for providing art guidance. The authors are also grateful for the support from the Center of Advanced Analysis & Gene Sequencing of Zhengzhou University and the Laboratory Animal Center, Zhengzhou University. We also thank the Academy of Medical Sciences of Zhengzhou University Translational Medicine platform. This work was supported by the National Natural Science Foundation of China (82302328), Henan Province Young and Middle-aged Health Science and Technology Innovation Outstanding Youth Talent Training Program (YQRC2024014), Major Science and Technology Special Project of Henan Province (221100310100), Central Plains Science and Technology Innovation Leading Talent Project (244200510020), Beijing Medical Award Foundation (YXJL-2023-0638-0046), Key Scientific research Program of Henan University (25A320034) and High-level Innovation Team of Wenzhou's "Ouyue talent Plan" (No. 2024R3003). Funded by the Innovation and Entrepreneurship Training Program of Zhengzhou University (2024cxcy087).

Author contributions

J.S., C.Z. and Y.Z. designed the experiments, analyzed the data and wrote the manuscript. Y.L., B.Y., and G.Z. synthesized microspheres for the detection and analysis of their physical and chemical characterization. B.H., J.L., K.W. and H.W. completed the animal experiment and imaging experiment. Y.W., Q.H. and L. Zongming completed the cytological experiments. X.S. carried out the photothermal experiments. K.R. and L. Zhen provided the DSA equipment and puncture instruments. All the authors discussed the results and approved the final version of the manuscript. P.W. and L.D. refined the manuscript.

Competing interests

The authors declare no competing interests.

Animal ethics

All procedures were approved by the Animal Care Committee of the First Affiliated Hospital of Zhengzhou University (ZZU-LA20210423[02]).

Additional information

Supplementary information The online version contains supplementary material available at https://doi.org/10.1038/s43246-025-00995-w.

Correspondence and requests for materials should be addressed to Jianzhuang Ren, Linyong Du, Yanan Zhao or Xinwei Han.

Peer review information *Communications Materials* thanks the anonymous reviewers for their contribution to the peer review of this work. A peer review file is available.